Small-scale structures in Boussinesq convection

Weinan E
School of Mathematics, Institute for Advanced Study, Princeton, New Jersey 08540

Chi-Wang Shu
Division of Applied Mathematics, Brown University, Providence, Rhode Island 02912

(Received 22 July 1992; accepted 18 June 1993)

Two-dimensional Boussinesq convection is studied numerically using two different methods: a filtered pseudospectral method and a high-order accurate ENO scheme. The issue whether finite time singularity occurs for initially smooth flows is investigated. In contrast to the findings of Pumir and Siggia who reported finite time collapse of the bubble cap, the present numerical results suggest that the strain rate corresponding to the intensification of the density gradient across the front saturates at the bubble cap. Consequently, the thickness of the bubble decreases exponentially. On the other hand, the bubble experiences much stronger straining and intensification of gradients at its side. As the bubble rises, a secondary front also forms from its tail. Together with the primary front, they constitute a pair of tightly bound plus and minus double vortex sheet structure which is highly unstable and vulnerable to viscous dissipation.

I. INTRODUCTION

In this paper, we present the results of a careful and detailed numerical study of the small-scale structures in two-dimensional Boussinesq convection in the absence of viscous effects. In particular, we address the issue of whether a finite time singularity can form out of a smooth initial data. Recently in their numerical study of the same problem,[1] Pumir and Siggia observed that the cap of a symmetric rising bubble (with smooth density variation) collapses in a finite time. In contrast, our results suggest that collapse of the bubble cap is a very unlikely candidate for finite time singularity formation. The strain rate associated with the intensification of the density gradient saturates at the cap, implying an exponential decay for the thickness of the cap. We note that the scaling argument in Ref. 2 also predicts an exponential increase of the density gradient at the cap. This is reminiscent of the situation found in vortex reconnection:[3–5] When two vortex tubes are brought together, the axial strain rate saturates and the core of the tubes undergoes enormous deformation to avoid reconnection (in the absense of viscosity). Thus the inviscid solution manages to escape from forming a finite time singularity. For the present problem, what prevented the collapse at the cap is the geometrical simplicity of the cap. While secondary instabilities are very likely to occur at the side of the bubble, we failed to find any mechanism to cause secondary perturbations at the cap which would in turn complicate the geometry there. We also found that as the bubble rises, a secondary front also forms from its tail. Together with the primary front, they constitute a pair of tightly bound plus and minus double vortex sheet structure which is highly unstable and vulnerable to viscous dissipation. The roll-up of the tail vortices packs together tightly these vortex sheet pairs.

There are two main motivations for the study of the two-dimensional Boussinesq convection. One comes from the potential relevance of this problem to the study of atmospheric and oceanographic turbulence, as well as other astrophysical situations where rotation and stratification play a dominant role. The second motivation comes from the fact that from a computational viewpoint, this is the simplest among the class of incompressible flows which exhibit vorticity intensification. In particular, it is an open question whether the baroclinic generation of vorticity leads to a finite time singularity. Such singularities, if exist, provide an effective mechanism for the cascade of energy to small scales. This scenario also provides a convenient basis for various turbulence theories which assume, in one form or another, that the (ensemble average of) rate of viscous dissipation of energy remains finite in the limit of vanishing viscosity, implying the occurrence of finite time singularities for abundance of Euler flows.[6]

There is a well-known analogy between the two-dimensional Boussinesq convection and the three-dimensional axisymmetric swirling flows:

$$\begin{aligned} &v_t+uv_r+wv_z+(1/r)uv=0,\\ &\omega_t+u\omega_r+w\omega_z-(1/r)u\omega-(1/r)(v^2)_z=0. \end{aligned} \tag{1}$$

Here, $\mathbf{u}=u\mathbf{e}_r+v\mathbf{e}_\theta+w\mathbf{e}_z$ is the velocity, $\omega=u_z-w_r$ is the azimuthal vorticity. Comparing (1) with (2)–(5), we see that the centrifugal force plays a similar role as the gravity, and the azimuthal circulation plays a similar role as the density. Grauer and Sideris[7] were the first to seek finite time singularities in this restricted class. Although their numerical result still remains inconclusive, it has stimulated a lot of recent work along the same direction, including the present study. Also of interest is the work of Caflisch[8] on singularity formation in the complex solutions of (1).

A related problem was studied earlier by Childress,[9] where he considered nearly two-dimensional Euler flows and derived effective equations governing their slow variation using contour averaging methods. Under a change of variables, the effective equation takes a form similar to the axisymmetric Euler equations with nonstandard connection between circulation, radius, and the angular velocity

 1070-6631/94/6(1)/49/10/$6.00

component. Childress went further to study numerically a simplified version of his effective equations and observed finite time singularities for the simplified model. This was interpreted as a signal for the re-three-dimensionalization of the original (nearly two-dimensional) flow.

This paper is organized as follows. In Sec. II, we formulate the problem and present some preliminary mathematical remarks. In Sec. III, we describe the numerical methods used to study this problem. The numerical results are presented in Sec. IV.

II. FORMULATION OF THE PROBLEM

The equations describing Boussinesq convections are the following:

$$\begin{aligned} &\rho_t+\mathbf{u}\cdot\nabla\rho=0,\\ &\mathbf{u}_t+\mathbf{u}\cdot\nabla\mathbf{u}+\nabla p=\begin{pmatrix}0\\ \rho\end{pmatrix},\\ &\nabla\cdot\mathbf{u}=0. \end{aligned} \tag{2}$$

Here, ρ is the density (usually this should be the temperature and denoted by θ or T, but we are accustomed to call it density, and therefore denote it by ρ), $\mathbf{u}=(u,v)$ is the velocity, p is the pressure. We have normalized the gravitational constant to be 1.

It is convenient to write (2) in the streamfunction–vorticity formulation:

$$\begin{aligned} &\rho_t+\mathbf{u}\cdot\nabla\rho=0,\\ &\omega_t+\mathbf{u}\cdot\nabla\omega=-\rho_x,\\ &-\Delta\psi=\omega. \end{aligned} \tag{3}$$

Here, ω is the vorticity, ψ is the streamfunction:

$$\omega=u_y-v_x,\quad u=-\psi_y,\quad v=\psi_x. \tag{4}$$

Introducing the material derivative $D_t=\partial_t+\mathbf{u}\cdot\nabla$, (3) becomes simply

$$D_t\rho=0,\quad D_t\omega=\rho_x. \tag{5}$$

It is straightforward to show that if the initial data $\mathbf{u}(x,y,0)=\mathbf{u}_0(x,y)$ and $\rho(x,y,0)=\rho_0(x,y)$ is smooth enough, then the solution to (2) exists and remains smooth for a short time. It is not clear whether any solution would lose its regularity at a finite time. However, following Beale, Kato, and Majda,[10] one can show that if a solution losses its regularity, then the density gradient has to blow up. More precisely, we have

Theorem: Define the norms:

$$\|f(\cdot)\|_m=\left(\sum_{\substack{\alpha_1,\alpha_2\geq 0\\ \alpha_1+\alpha_2\leq m}}\int_{R^2}\left|\frac{\partial^{\alpha_1+\alpha_2}f}{\partial x^{\alpha_1}\partial y^{\alpha_2}}\right|^2 dx\,dy\right)^{1/2},$$

$$|f(\cdot)|_\infty=\max_{(x,y)\in R^2}|f(x,y)|.$$

Assume that for some $m>2$, $\|\mathbf{u}(\cdot,0)\|_m+\|\rho(\cdot,0)\|_m$ is finite, but there exists a T^* such that $\|\mathbf{u}(\cdot,T^*)\|_m+\|\rho(\cdot,T^*)\|_m=+\infty$. Then

$$\int_0^{T^*}|\omega(\cdot,t)|_\infty dt=+\infty \tag{6}$$

and

$$\int_0^{T^*}\int_0^t|\rho_x(\cdot,s)|_\infty ds\,dt=+\infty. \tag{7}$$

Proof: We will only give a sketch of the proof since it follows closely the argument of Beale, Kato, and Majda.[10] We will use C to denote a generic constant.

Straightforward energy estimates lead to

$$\frac{d}{dt}\|\rho(\cdot,t)\|_m^2\leq|\nabla\mathbf{u}(\cdot,t)|_\infty\|\rho(\cdot,t)\|_m^2,$$

$$\frac{d}{dt}\|\mathbf{u}(\cdot,t)\|_m^2\leq|\nabla\mathbf{u}(\cdot,t)|_\infty\|\mathbf{u}(\cdot,t)\|_m^2+\|\rho(\cdot,t)\|_m^2.$$

The logarithmic Sobolev inequality gives us, for $m\geq 2$

$$|\nabla\mathbf{u}(\cdot,t)|_\infty\leq C|\omega(\cdot,t)|_\infty[1+\log\|\mathbf{u}(\cdot,t)\|_m].$$

Therefore, if we let

$$y(t)=\|\rho(\cdot,t)\|_m^2+\|\mathbf{u}(\cdot,t)\|_m^2,$$

we have

$$\dot{y}(t)\leq C|\omega(\cdot,t)|_\infty[1+\log y(t)]y(t).$$

Solving this differential inequality, we get

$$y(t)\leq e^{\exp[C\int_0^t|\omega(\cdot,s)|_\infty ds]}y(0).$$

On the other hand, since $D_t\omega=-\rho_x$, we have

$$\frac{d}{dt}|\omega(\cdot,t)|_\infty\leq|\rho_x(\cdot,t)|_\infty.$$

Hence,

$$|\omega(\cdot,t)|_\infty\leq\int_0^t|\rho_x(\cdot,s)|_\infty ds+C$$

and

$$y(t)\leq e^{\exp[C\int_0^t\int_0^s|\rho_x(\cdot,\tau)|_\infty d\tau\,ds]}y(0).$$

Since $y(0)$ is finite, we conclude that if $y(T^*)=+\infty$, then (6) and (7) hold.

Remark: Eqs. (6) and (7) tell us the minimum rate of a blowup: If $\max|\omega|$ blows up like $c_1(T^*-t)^{-\alpha}$, and $\max|\rho_x|$ blows up like $c_2(T^*-t)^{-\beta}$, then $\alpha\geq 1,\beta\geq 2$. Since (2) is invariant under the following scaling transformations:

$$x\to\lambda^2 x,\quad t\to\lambda t,\quad \rho\to\rho,\quad \mathbf{u}\to\lambda\mathbf{u},$$

a self-similar blowup implies $\alpha=1$, $\beta=2$. At this level, it is consistent with the findings of Pumir and Siggia.

III. THE NUMERICAL METHODS

Computing singular or nearly singular solutions is a difficult task, particularly so in the context of incompressible flows. To obtain maximum information one has to push the numerical method to the point where the flow is only marginally resolved. In this situation any numerical

method is likely to exhibit its own artifacts. Such numerical artifacts may not go away under simple mesh refinement checks, and they do not necessarily manifest themselves in scales comparable to the grid size. Therefore, there is a real danger of being misled by a particular numerical result. To avoid this, we have solved (2) using two different numerical methods: a Fourier-collocation method and an ENO scheme. When the solution develops large gradients, the Fourier-collocation method usually exaggerates the situation, whereas the ENO scheme tends to smear out the large gradients. By comparing the numerical results using the two different methods, we can be more sure of what phenomena are likely to be physical. Below we will describe separately the two methods.

A. Spectral method with smoothing

This is the standard Fourier-collocation method[11] with smoothing or dealiasing. Roughly speaking, the differentiation operator is approximated in the Fourier space, while the nonlinear operations such as multiplications are done in the physical space. We used the intrinsic Cray FFT routines which considerably enhanced the performance of the code.

Since the solutions have large gradients, it is crucial to add filters to the spectral method in order that the numerical solutions do not degrade catastrophically if some part of the steep gradients are not adequately resolved. A robust way of adding the filters[12] is to replace the Fourier multiplier ik_j for the differentiation operator ∂_{x_j} by $ik_j\varphi(|k_j|)$, where

$$\varphi(k)=e^{-\alpha(k/N)^{m_f}}, \quad \text{for } |k|\leqslant N. \tag{8}$$

Here, N is the numerical cutoff for the Fourier modes, m_f is the order of the filter, and α is chosen so that $\varphi(N)=e^{-\alpha}=$machine accuracy. The machine accuracy on Cray YMP with single precision is roughly 10^{-14}. Denote by F and F^{-1}, respectively, the forward and backward Fourier transform operators, then the numerical derivative is evaluated as

$$D_N f=F^{-1}[ik\varphi(|k|)]Ff. \tag{9}$$

The accuracy of such an approximation scheme depends on the parameter m_f. For smooth functions $f(x)$, we have

$$\|f'(x)-D_N f(x)\|=O(N^{-m_f}). \tag{10}$$

We will denote the Fourier-collocation method with m_fth order filter as SPmf. Unless otherwise stated, the results presented in Sec. IV B were computed with $m_f=10$.

B. The ENO scheme

The essentially nonoscillatory (ENO) scheme is used for the convection (spatial) part of the flow. We use ENO schemes based on point values and numerical fluxes, developed by Shu and Osher in Refs. 13–15. Some interesting calculations for incompressible flows using ENO schemes can be found in Ref. 16.

To apply ENO approximations, the equation is first written in a conservation form. For example, the first equation in (3) is written as

$$\rho_t+(u\rho)_x+(v\rho)_y=0. \tag{11}$$

The ENO operator is then applied to each of the conservative derivatives in a dimension-by-dimension fashion: when approximate $(u\rho)_x$, y is viewed as being fixed. Unlike the compressible flow, the incompressible flow equations are naturally written in characteristic form. Thus no expensive characteristic decomposition is needed. Upwinding can be simply determined by the signs of u and v.

We shall only briefly describe the approximation of a single derivative, say f_x. More details can be found in Refs. 13–15.

The conservative approximation is of the form:

$$(f_x)_j\equiv=(1/\Delta x)(\hat{f}_{j+1/2}-\hat{f}_{j-1/2}) \tag{12}$$

which, for rth order ENO scheme, approximates the derivative to rth order:

$$(1/\Delta x)(\hat{f}_{j+1/2}-\hat{f}_{j-1/2})=f_x|_{x=x_{j+1/2}}+\mathcal{O}(\Delta x^r), \tag{13}$$

where the numerical flux $\hat{f}_{j+1/2}$ is obtained by interpolating the point values of f on a stencil of $r+1$ consecutive grid points. The stencil is chosen inductively as follows. For $r=1$, we choose the stencil to be $[j-1,j]$ or $[j,j+1]$ depending on the sign of u. For $r>1$, left or right neighboring points are added to the stencil at the previous level $r-1$, according to the absolute value of the divided differences they each give. In most of our calculations, we used $r=3$. We will denote this method by ENO3. Notice that the scheme is actually $r+1$th order in L_1 norm. That is, the third-order ENO scheme we use is actually fourth order accurate in the L_1 norm.

The potential equation in (3) is solved with a fourth order central differencing (implemented in the Fourier space via FFT) plus a fourth-order exponential filtering in the Fourier space described above. This guarantees fourth order accuracy and in most cases avoids instability. We are not sure whether ENO should or can be applied to this potential solver, since it is an elliptic equation with possibly singular right-hand side. Unlike in the compressible case, some small oscillations can still be seen in the ENO solution, probably due to this potential solver.

For the temporal discretization, we used Runge–Kutta methods of various order designed in Ref. 14. No major difference between the third, fourth, and fifth-order methods were found in the numerical results. It seems to be a general fact that temporal accuracy is much less important than the spatial accuracy. We used the third-order version most often since it only requires three auxiliary arrays, whereas the fourth-order version requires five auxiliary arrays. We take initial data that is periodic with period D where $D=[0,2\pi]\times[0,2\pi]$. Although periodic boundary conditions are rather unphysical for the convection problem, we expect that it does not matter for what we are interested in, which is the small-scale structures. The re-

sults reported below were computed using CFL equal to 0.5. This is very much within the stability region of these methods.

In the calculations reported below, energy is always conserved to within one-tenth of a percent. It is much more difficult to preserve the maximum and minimum of the density. The ENO scheme gives far better result on that [see Figs. 5(a) and 5(b)].

We point out that our experience favors strongly the use of high-order schemes because of their small dispersive errors. In a marginally resolved situation, even though the filtered spectral method does generate small oscillations near the front where the density experiences a jump, the oscillations are effectively localized near the front. This is because the spurions numerical oscillations travel at roughly the right speed which is the speed of the front. The higher the order of the filter, the more accurate the propagation speed, the more localized the oscillations. Of course eventually the Gibbs phenomena prevail and the numerical result becomes noise.

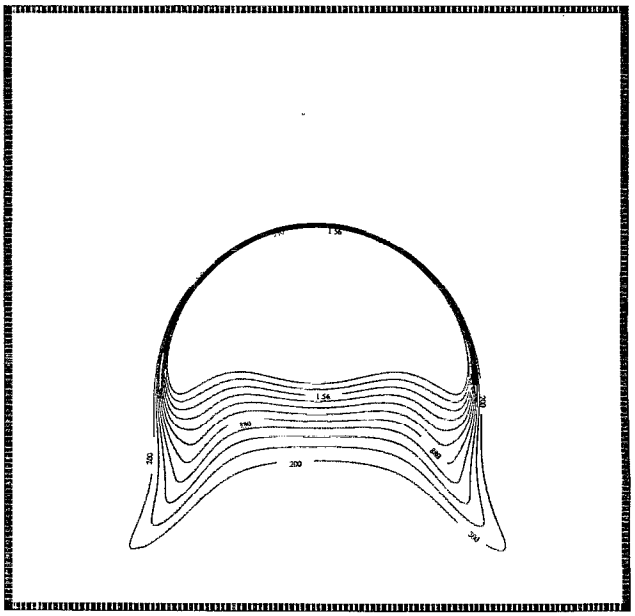

FIG. 1. Density contour at $t=1.6$ for initial data (14) computed on a 512^2 grid. A front has formed at this time.

IV. NUMERICAL RESULTS

A. Formation of the front

We have numerically integrated (2) with a variety of initial data. The initial density is usually a perturbation of the uniform state, and the perturbations are localized in each period. The early time evolution of such flows is characterized by the formation of a front across which density varies sharply. As time evolves the front gets increasingly sharp and the tail starts to roll up. Figures 1–3 present the time development of such events for the initial data

$$\omega(x,y,0)=0,$$
$$\rho(x,y,0)=50\rho_1(x,y)\rho_2(x,y)[1-\rho_1(x,y)], \tag{14}$$

where

$$\rho_1(x,y)=\exp\left(1-\frac{\pi^2}{\pi^2-x^2-(y-\pi)^2}\right),$$
$$\text{if } x^2+(y-\pi)^2\leqslant\pi^2,$$
$$=0 \quad \text{otherwise},$$
$$\rho_2(x,y)=\exp\left(1-\frac{(1.95\pi)^2}{(1.95\pi)^2-(x-2\pi)^2}\right),$$
$$\text{if } |x-2\pi|<1.95\pi,$$
$$=0 \quad \text{otherwise}.$$

Figure 1 is the density contour at $t=1.6$ computed using SP10 on a 512^2 grid. At this time, the flow looks roughly like a rising bubble. In Figs. 2(a) and 2(b) we present, respectively, the contours of density and vorticity at $t=3$. By now the outer boundary of the bubble has become a sharp front. We notice that as the bubble rises, it leaves behind a long and thin filament of light fluid. This is a check on the amount of numerical diffusion present in the scheme. A low-order method with numerical viscosity (needed to stabilize the front) will destroy the thin filament. From Fig. 2(b) we see that most of the vorticity resides on the front, the rest of the flow domain has very little vorticity. This fact is more drastically displayed in Figs. 3(a) and 3(b) where we plot, respectively, the slice of ω and ρ_x at $y=\pi$. Since ω and $-\rho_x$ have the same sign, from the vorticity equation (3) we see that the vorticity peaks will be increasingly and monotonically sharper. The development of the front is most clearly seen in Fig. 4, which displays the evolution of the density along the symmetry axis $x=\pi$ at times $t=0.5$, 1, 1.5, 2, and 2.5. It shows clearly the formation of a front, similar to the formation of shock fronts in the solutions of the Burgers equation. At $t=2.5$, SP10 on the 512^2 grid is not resolving the flow and small numerical oscillations appear on the profile. However, the numerical oscillations are not present on the refined grid 1024^2. The result of the latter calculation is superimposed in Fig. 4 on the solution of the 512^2 grid.

These results, particularly Fig. 2(a) motivate the following question: Is it possible that the density develops jump discontinuities at the entire front or part (not a single point) of the entire front at the same time? For this to happen, fluids with intermediate densities should be suddenly swept to the back of the bubble. Clearly this needs infinite velocity whereas all of our numerical results give velocities that are very well bounded.

Before ending this subsection, we present the comparison of the numerical results computed using the two different methods described in Sec. III. Figures 5(a) and 5(b) display, respectively, the time history of the maximum and minimum density computed using SP10 on 256^2, 512^2, and 1024^2 grids, and ENO3 on the 512^2 grid. These quantities should be conserved by the exact solutions. As expected, ENO does a much better job in avoiding over-

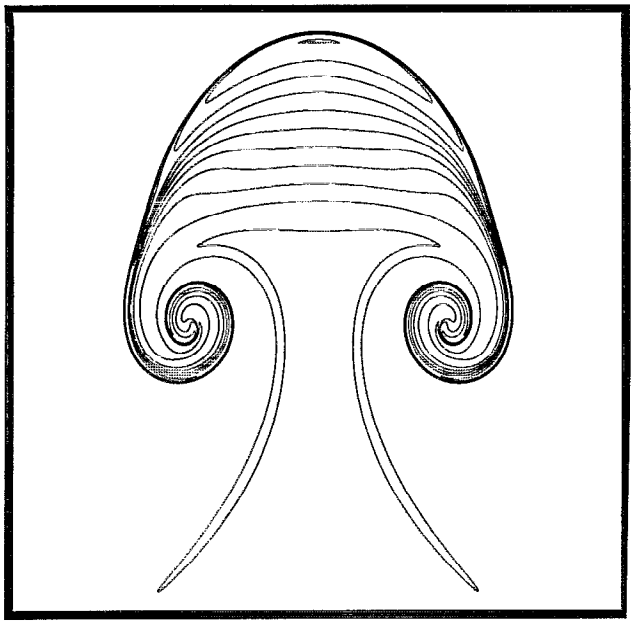

(a)

(b)

FIG. 2. (a) Density contour at $t=3$ for initial data (14) computed on a 1500^2 grid. The bubble cap is unstable according to (A14). But no small-scale instability at the cap is seen here. (b) Vorticity contour at the same time as in (a).

shoots and undershoots. Figure 5(c) compares the numerical results for ρ at $y=\pi$, $t=2.5$, computed using SP10 and ENO3 on 512^2 grid. The result of SP10 undershoots much more than the result of ENO3, although the latter also contains some small numerical oscillations. On the other hand, although not shown here, ENO is usually less accurate than the Fourier-collocation method and contains more numerical dissipation.

B. Evolution of the bubble cap

When the bubble rises, lighter fluid has larger acceleration and heavier fluid has smaller acceleration. This results in the formation of fronts. However, once the front is formed, pressure gradient becomes important across the front. In fact, as is shown in Figs. 6(a) and 6(b), the increasing pressure gradient may reverse the initial picture.

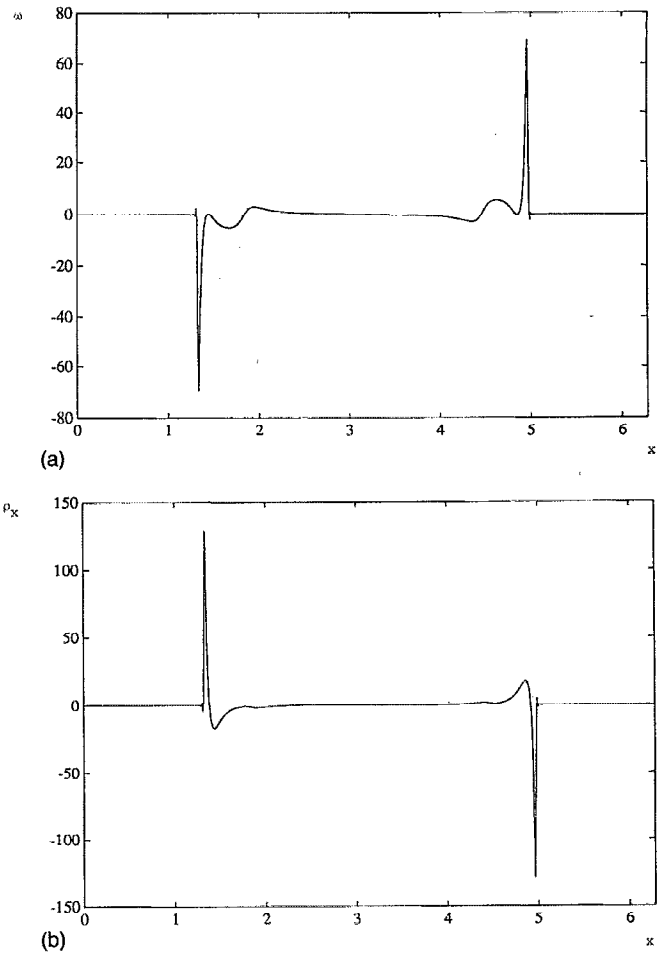

FIG. 3. (a) The slice of ω at $y=\pi$, $t=2.5$. (b) The slice of ρ_x at $y=\pi$, $t=2.5$.

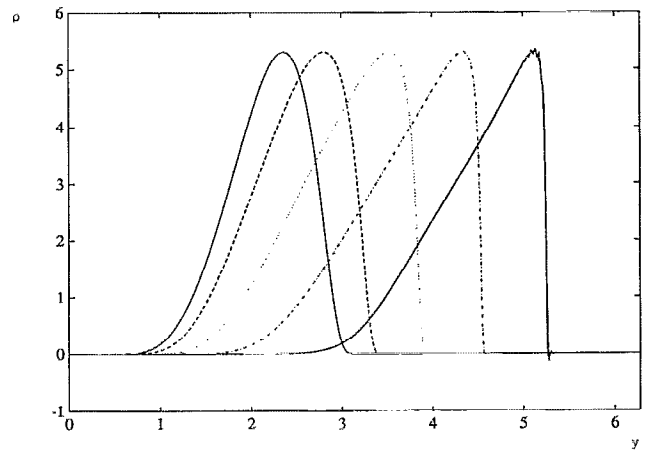

FIG. 4. Evolution of density along the symmetry axis $x=\pi$ at $t=0.5$, 1, 1.5, 2, and 2.5, computed using SP10 on a 512^2 grid. The result at $t=2.5$ computed on a 1024^2 grid is also superimposed. Notice that the small numerical oscillations disappear on the refined grid.

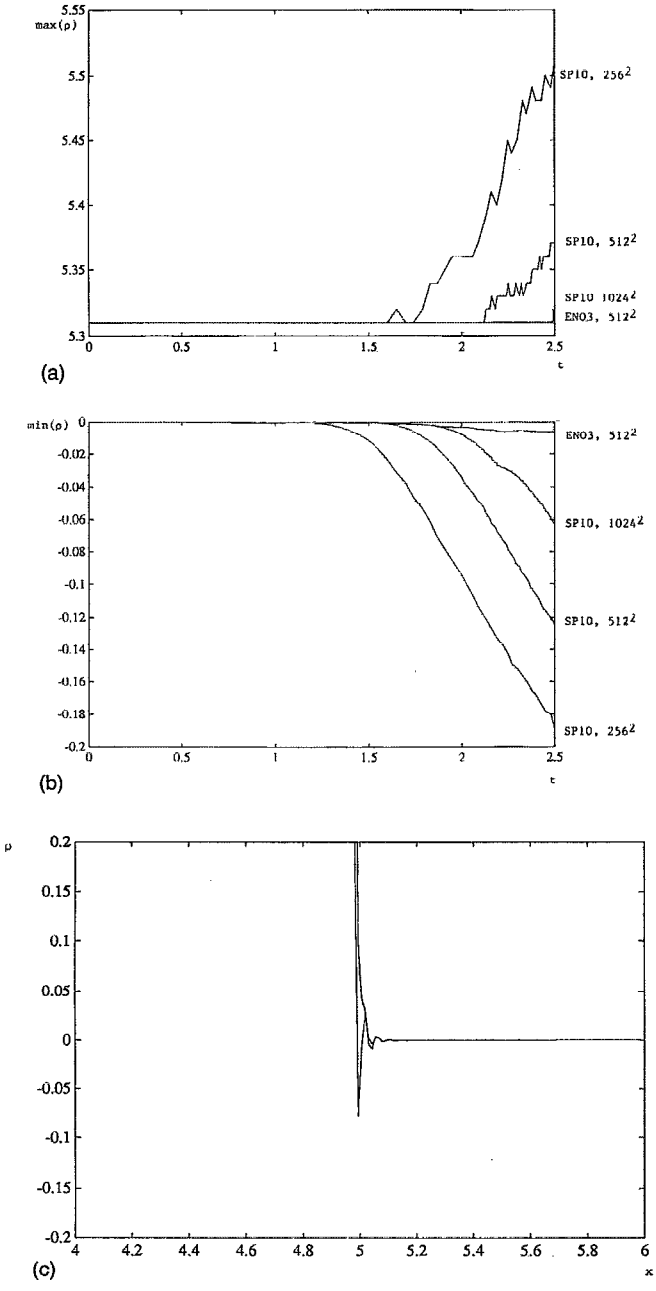

FIG. 5. (a) Time history of the maximum density from different computations. From top to bottom: SP10 on the 256^2 grid, SP10 on the 512^2 grid, SP10 on the 1024^2 grid, and ENO3 on the 512^2 grid. (b) Time history of the minimum density from different computations. From bottom to top: SP10 on the 256^2 grid, SP10 on the 512^2 grid, SP10 on the 1024^2 grid, and ENO3 on the 512^2 grid. (c) Comparison of the numerical results for ρ across the front at $y=\pi$, $t=2.5$ for two different methods, SP10 and ENO3, both on the 512^2 grid. ENO3 has less numerical oscillation.

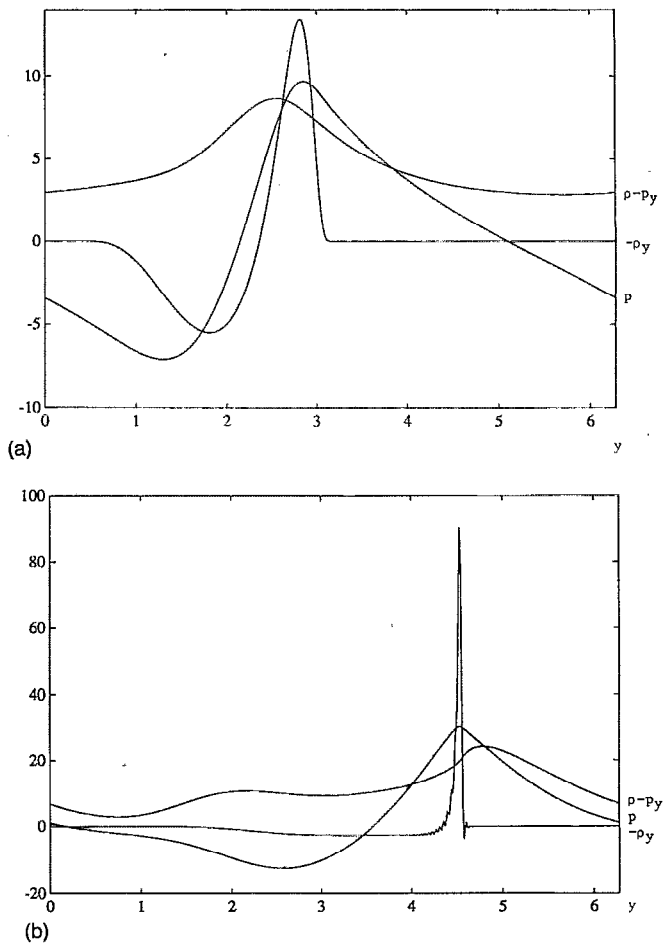

FIG. 6. (a) Slice of $-\rho_y$, p, and $\rho-p_y$ at $t=0.5$ along the symmetry axis $x=\pi$. The acceleration $\rho-p_y$ decreases across the front. (b) Slice of $-\rho_y$, p, and $\rho-p_y$ at $t=2$ along the symmetry axis $x=\pi$. The acceleration $\rho-p_y$ now increases across the front.

In Figs. 6(a) and 6(b), we plot the slice of $-\rho_y$, p, and the acceleration $\rho-p_y$ along the symmetry axis $x=\pi$ at two different times $t=0.5$ and $t=2$. At $t=0.5$, the acceleration $\rho-p_y$ decreases across the front, whereas at $t=2$ it increases across the front. (The density ρ always decreases across the front, see Fig. 4.) This implies that the velocity difference between the fluid particles at the tip and the back of the front will not increase further after $t=2$, assuming that the picture remains valid.

At the symmetry axis we have

$$\rho_t+v\rho_y=0,$$
$$u=0, \tag{15}$$
$$v_t+vv_y=\rho-p_y.$$

On the other hand, pressure satisfies

$$\rho_y-\Delta p=u_x^2+v_y^2+2u_yv_x, \tag{16}$$

which reduces to

$$\rho_y-p_{yy}-p_{xx}=2v_y^2 \tag{17}$$

at the symmetry axis.

Let $\xi=\rho_y$, $\eta=v_y$. Then we have, at the symmetry axis,

$$D_t\xi=-\xi\eta,$$
$$D_t\eta=p_{xx}+\eta^2. \tag{18}$$

Let us examine this in a bit more detail. Consider two fluid particles at the front and the symmetry axis: (π,y_1) and (π,y_2). Assume that $0<Y=y_1-y_2\ll 1$. We have

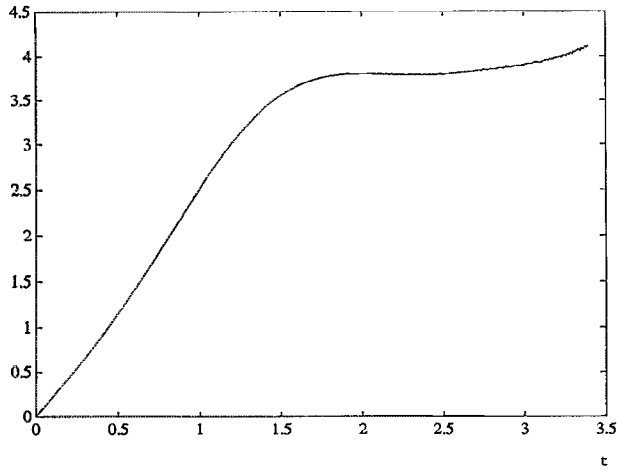

FIG. 7. Time history of $|u_x|+|v_x|+|u_y|+|v_y|$ at the cap. This is roughly twice the strain rate. It saturates from $t=1.7$ and only increases slightly after $t=3$.

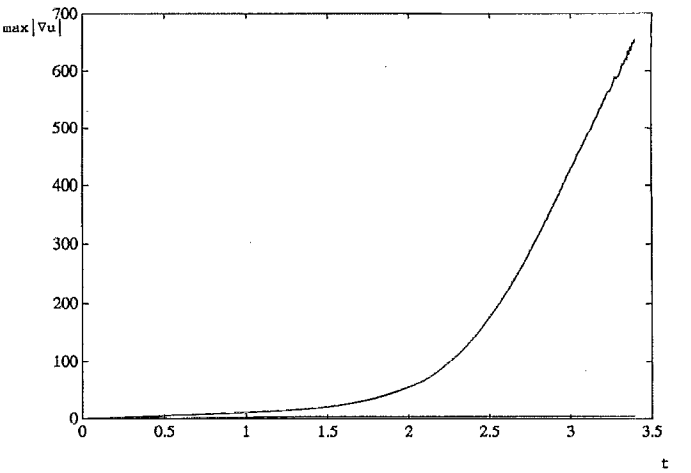

FIG. 8. Comparision of the (time history of) maximum of $|u_x|+|v_x|+|u_y|+|v_y|$ over the whole domain and at the cap. The bubble is stretched much more at the side than the cap.

$$\ddot{Y}=(\rho-p_y)(\pi,y_1,t)-(\rho-p_y)(\pi,y_2,t)$$
$$=Y(\rho-p_y)_y(\pi,y^*,t), \tag{19}$$

where $y_2\leqslant y^*\leqslant y_1$. Assume for the moment that p_{xx} is negligible compared with p_{yy}. Then

$$\ddot{Y}\approx 2Yv_y^2(\pi,y^*,t). \tag{20}$$

Since

$$v_y\approx\frac{1}{y_1-y_2}\frac{d}{dt}(y_1-y_2)=\frac{\dot{Y}}{Y}, \tag{21}$$

we get

$$\ddot{Y}\approx 2(\dot{Y}/Y)^2Y. \tag{22}$$

Consequently, we have

$$\left(\frac{\dot{Y}}{Y}\right)^{\cdot}=\frac{1}{Y^2}[Y\ddot{Y}-(\dot{Y})^2]=\left(\frac{\dot{Y}}{Y}\right)^2>0. \tag{23}$$

This implies that for some constants c_1,c_0, we have

$$Y(t)>e^{-(c_1t+c_0)} \tag{24}$$

precluding the possibility of having a finite time collapse at the bubble cap.

This conclusion can also be drawn directly from (18). If $p_{xx}+\eta^2>0$, then η is bounded from below. Therefore, $\xi(t)=e^{-\int^t\eta(s)ds}\xi(0)$ does not blow up. (Here we neglected the Lagrangian coordinate of the fluid particles.) Hence, for the collapse to occur, it is necessary that at some point of the symmetry axis and the front,

$$p_{xx}<-v_y^2. \tag{25}$$

This means that variations along the front should be comparable to variations across the front. In other words, the front develops instabilities with wavelength comparable to the thickness of the front. Here lies the key difference between the calculations presented in this paper and the ones in Ref. 1.

To examine this issue in detail, we need to ask two questions. One is whether the front is indeed unstable to small-scale perturbations. The other is the source of perturbations: What causes the front to start to wrinkle?

The linear stability analysis along the lines Refs. 1 and 17 is presented in the Appendix. Let us check whether the instability criterion (A14) is satisfied at $t=3$. From Fig. 2(a), we haved roughly $R/\delta>45$, $\tilde{g}\approx 2.65$, $s\approx 1.9$. So the left-hand side of (A14) is about 2.1×10^3, and the right-hand side is about 8.8×10^3. Therefore the bubble cap is unstable, according to (A14).

However, in all the calculations we have done for this and other data, we have never observed small-scale instability at the cap. Even for the bubble shown in Fig. 10 at $t=3.16$, for which $R/\delta>100$, and the ratio of the right-hand side of (A14) to the left-hand side is larger than 1.8×10^2, no small-scale instability was observed at the cap.

We also tried different sets of initial data. Some of the numerical results were reported in Ref. 18. Again, no

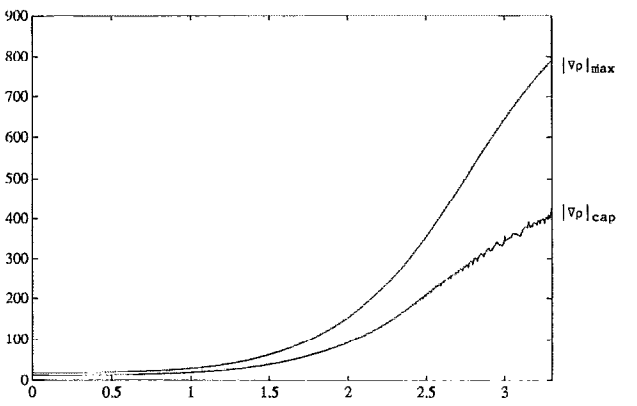

FIG. 9. Comparision of the (time history of) maximum of $|\rho_x|+|\rho_y|$ over the whole domain and at the cap. This also shows that the bubble cap is less dangerous than the side.

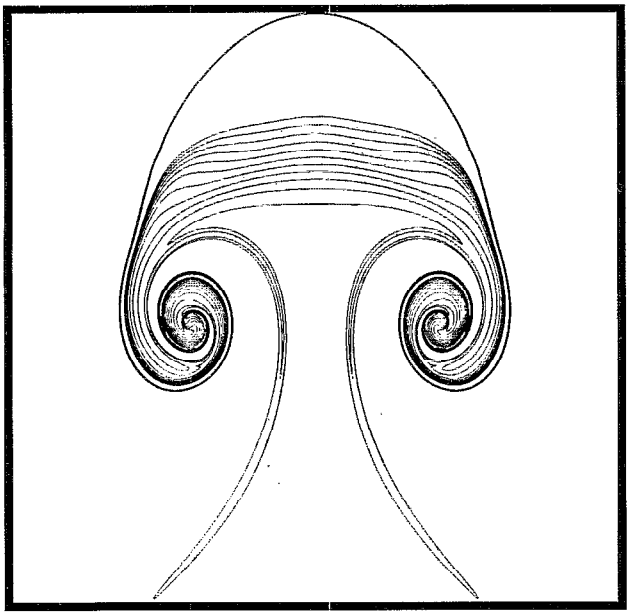

FIG. 10. Density contour at $t=3.16$ shows the formation of a second front which runs parallel to the primary front but bifurcates from it at an inflection point (see text), SP10 on a 1500^2 grid.

small-scale instabilities were observed at the cap even though the bubble cap in Figs. 9(b) and 11 of Ref. 18 were unstable, according to (A14).

C. Other aspects of the flow

There is strong evidence that the side of the bubble is much more dangerous than the cap. This can be seen partly from Figs. 7–9. Figure 7 shows the time history of

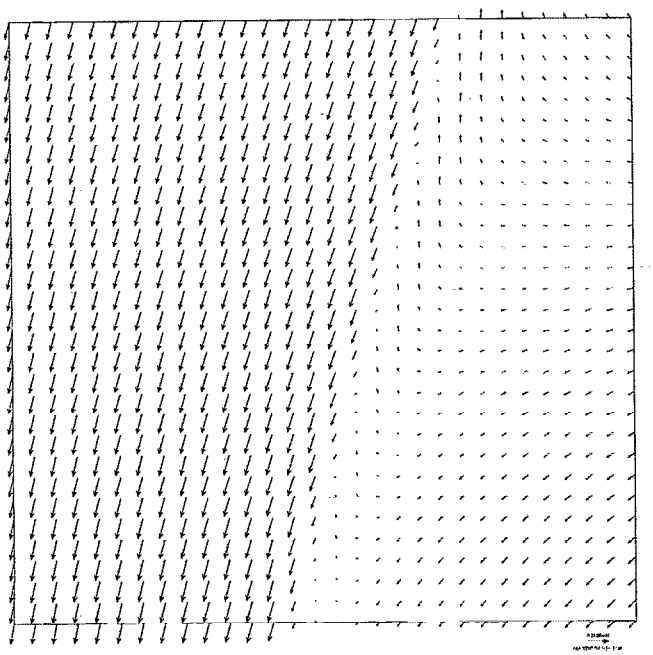

FIG. 11. Velocity field nearby the inflection point.

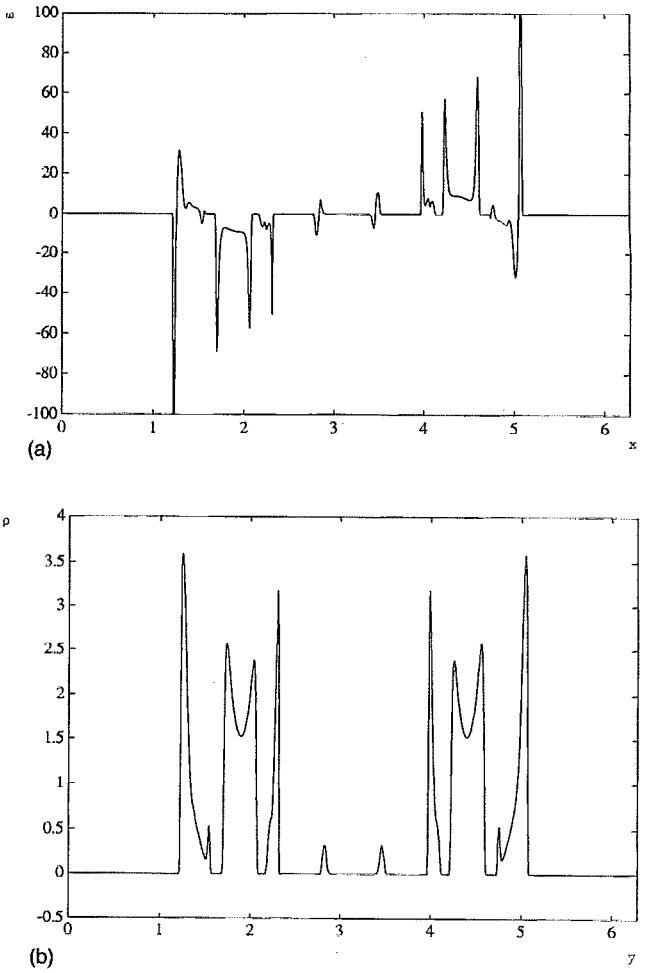

FIG. 12. (a) A cut of vorticity profile through the roll at $t=3.16$. The outer-most peaks are accompanied by peaks in the opposite direction. This is an illustration that the primary front and the secondary front form a pair of tightly bound plus and minus vortex sheets. (b) A cut of the density profile through the roll at $t=3.16$.

the maximum of $(|u_x|+|u_y|+|v_x|+|v_y|)$ over the domain and compared to its value at the cap (the flat curve). This maximum is attained at the bottom of the front where the front has been stretched the most. The maximum of the local strain rates, the eigenvalues of the strain matrix, shows exactly the same behavior. At $t=3.4$, the maximum local strain rate is about 520. In comparison, the strain rate at the cap, shown in Fig. 8, saturates starting from $t=1.7$ at a value of about 1.9 and only increases slightly after $t=3$. A similar comparison is made in Fig. 9 for the density gradient $|\rho_x|+|\rho_y|$. The maximum of the density gradient occurs at the side of the bubble (between the cap and the inflection point in Fig. 10, see below).

The evolution of the front is rather complicated. After the formation of the primary front, a secondary front also forms from the tail vortices. This is clearly shown in Fig. 10. This secondary front runs almost parallel to the primary front to a point where it bifurcates from the primary front. This point is also characterized by the fact that the front is most flat there. It can be seen from Fig. 10 that this point is becoming an inflection point for the front. We also

show in Fig. 11 the velocity field nearby this point. Preliminary calculations suggest that the front starts to roll up here, but so far we have not been able to resolve the subsequent roll-ups with enough confidence. In terms of vorticity, the primary front corresponds to a vortex sheet (or almost a vortex sheet, to be more precise). The secondary front corresponds to another vortex sheet, but the vorticity has the opposite sign. So we have a pair of tightly bound plus and minus vortex sheets coming out of the roll. These are very much analogous to the canonical structures in turbulence suggested by Chorin:[19] tightly folded hairpins or antiparallel vortex filaments. Indeed, small perturbations in the third dimension will break them into hairpin vortices. To illustrate these sheet pairs we plot in Fig. 12(a) a cut of vorticity profile through the roll. We can see clearly that the outermost vorticity peaks are accompanied by peaks in the opposite direction. This also happens for several other vorticity peaks. The corresponding density profile is shown in Fig. 12(b).

Such structures are very unstable and vulnerable to viscous dissipation. Indeed, experimental results[17] provide overwhelming evidence that the lower part of the bubble is much easily destroyed by perturbations, whereas near the cap, the shape of the bubble is very easily maintained.

ACKNOWLEDGMENTS

We are grateful to Steve Childress, Jonathan Goodman, Andy Majda, and Mike Shelley for numerous stimulating discussions. We also want to thank Tom Sideris and Eric Siggia for communicating their results to us. The work of E was supported by ARO Contract Nos. DAAL03-89-K-0039, AFOSR-90-0090, and NSF Grant No. DMS-9100383. The work of Shu was supported by ARO Contract No. DAALO3-91-G-0123, NASA NAG1-1145, and NAS1-18605 while in residence at ICASE. The numerical computation reported here was done on the Cray-YMP computers at the Pittsburgh Supercomputing Center.

APPENDIX: LINEAR STABILITY OF THE BUBBLE CAP IN A STRAINING FLOW

Here we give a brief presentation of the linear stability analysis of a bubble near the cap in a straining flow using the Boussinesq approximation. We follow closely Refs. 17 and 1.

We begin with the Boussinesq equations

$$\rho_t+(\mathbf{u}\cdot\nabla)\rho=0,$$
$$\rho_0[\mathbf{u}_t+(\mathbf{u}\cdot\nabla)\mathbf{u}]+\nabla p=\rho\mathbf{g}, \tag{A1}$$

where $\mathbf{g}=(0,1)$. As in Ref. 1, we study the idealized situation where the density jumps from $\rho_0+\rho$ to ρ_0 across the bubble surface, and view the small thickness of the bubble front as a cutoff for the wavelength of possible perturbations. The radius of curvature near the cap is assumed to be R. In polar coordinates (r,θ) the perturbed bubble can be represented in the following form:

$$r=R+\eta(\theta,r,t). \tag{A2}$$

We will assume that the flow is irrotational both inside and outside the bubble. This is a reasonable assumption since almost all vorticity is concentrated at the front, see Figs. 2(b) and 3(a). Introducing the velocity potentials φ_1 and φ_2 inside and outside the bubble, respectively, we have $\varphi_1=\Phi+\varphi_1'$, $\varphi_2=\Phi+\varphi_2'$, and

$$-\Delta\varphi_1=0, \quad -\Delta\varphi_2=0, \tag{A3}$$

where Φ is the velocity potential for the unperturbed bubble. We assume that the unperturbed velocity $u_0=\nabla\Phi$ is a straining flow near the cap:

$$u_0\approx sx, \quad v_0\approx -s(y-1), \tag{A4}$$

where s is the strain rate.

The dynamic condition, given by Bernoulli's law, states that $\rho_0(\varphi_t+\frac{1}{2}|\nabla\varphi|^2)-\rho g$ should be continuous across the interface. Neglecting higher-order terms in φ_1' and φ_2', this gives

$$\rho_0\left(\varphi_{2t}'+\frac{u_0}{R}\varphi_{2\theta}'\right)=\rho_0\left(\varphi_{1t}'+\frac{u_0}{R}\varphi_{1\theta}'\right)-\rho g\eta\cos\theta. \tag{A5}$$

We also have the kinematic condition which states that fluid particles at the surface flow with the velocity of the surface $r=1$:

$$\eta_t+\frac{u_0}{R}\eta_\theta+\frac{\eta}{R\sin\theta}\frac{\partial}{\partial\theta}(u_0\sin\theta)=\frac{\partial\varphi_1'}{\partial r}=\frac{\partial\varphi_2'}{\partial r}. \tag{A6}$$

Near the cap, we get the following set of equations using $u_0\approx sx\approx sR\theta$, $\xi=R\theta$:

$$\eta_t+s\xi\eta_\xi+2s\eta=\left.\frac{\partial\varphi_1'}{\partial y}\right|_{y=1},$$
$$\rho_0(\varphi_{2t}'+s\xi\varphi_{2\xi}')=\rho_0(\varphi_{1t}'+s\xi\varphi_{1\xi}')-\rho g\eta, \tag{A7}$$
$$\left.\frac{\partial\varphi_1'}{\partial y}\right|_{y=1}=\left.\frac{\partial\varphi_2'}{\partial y}\right|_{y=1}.$$

Let $z=y-1$, $\eta=A(t)e^{in\xi}$, $\varphi_1'=B_1(t)e^{n(i\xi+z)}$, $\varphi_2'=B_2(t)e^{n(i\xi-z)}$. From (A7) we have

$$B_1=-B_2=B,$$
$$\dot{A}+2sA=nB,$$
$$\rho_0\dot{B}_2=\rho_0\dot{B}_1-\rho gA, \tag{A8}$$
$$\dot{n}=-sn.$$

Hence, we get

$$\dot{A}=-2sA+nB,$$
$$\dot{B}=(\rho g/2\rho_0)A=\tilde{g}A. \tag{A9}$$

Since we expect that high wave-number modes will be most unstable, we solve (A9) using WKB approximation. Let

$$A(t)=\exp\left(\int_0^t f(\tau)d\tau\right). \tag{A10}$$

From (A8) we have

$$n(t)=n_0e^{-st}, \tag{A11}$$

$$f(t)=\sigma e^{-(s/2)t}-(s/4)s+\text{correction}, \tag{A12}$$

where $\sigma^2=n_0\tilde{g}$.

The maximum growth rate is

$$A=\left(\frac{5}{4}\frac{s}{\sigma}\right)^{5/2}e^{(2\sigma/s)-(5/2)}, \tag{A13}$$

which is attained at $t^*=-(2/s)\ln[(5/4)(s/\sigma)]$.

The finite thickness of the front presents a ultraviolet cutoff for the available modes. In Ref. 1, this cutoff is chosen to be $n_0=R/\delta$ where δ is the thickness of the front. Pumir and Siggia call the bubble cap unstable if the maximum amplification factor is larger than R/δ. In the present context, their instability criterion reads

$$\frac{R}{\delta}\left(\frac{4}{5}\frac{\sigma_c}{s}\right)^{5/2}\leqslant\exp\left\{\frac{2\sigma_c}{s}-\frac{5}{2}\right\}, \tag{A14}$$

where $\sigma_c=(R\tilde{g}/\delta)^{1/2}$.

[1] A. Pumir and E. D. Siggia, "Development of singuler solutions to the axisymmetric Euler equations," Phys. Fluids A **4**, 1472 (1992).

[2] X. Wang and A. Bhattacharjee, "Is there a finite-time singularity in axisymmetric Euler flows?," in *Toplogical Aspects of the Dynamics of Fluids and Plasmas*, edited by H. K. Moffatt *et al.* (1992), pp. 303–308.

[3] C. Anderson and C. Greengard, "The vortex ring merger problem at infinite Reynolds number," Commun. Pure Appl. Math. **42**, 1123 (1989).

[4] A. Pumir and E. D. Siggia, "Collapsing solutions to the 3-D Euler equations," Phys. Fluids A **2**, 220 (1990).

[5] M. J. Shelley, D. E. Meiron, and S. A. Orszag, "Dynamical aspects of vortex reconnection of perturbed anti-parallel vortex tubes," J. Fluid Mech. **246**, (1993).

[6] A. Majda, "Vorticity, turbulence, and acoustics in fluid flow," SIAM Rev. **33**, 349 (1991).

[7] R. Grauer and T. Sideris, "Numerical computation of 3D incompressible ideal fluids with swirl," Phys. Rev. Lett. **67**, 3511 (1991).

[8] R. Caflisch, "Singularity formation for complex solutions of the 3D incompressible Euler equations," preprint (1992).

[9] S. Childress, "Nearly two-dimensional solutions of Euler's equations," Phys. Fluids **30**, 944 (1987).

[10] J. T. Beale, T. Kato, and A. Majda, "Remarks on the breakdown of smooth solutions for the 3-D Euler equations," Commun. Math Phys. **94**, 61 (1984).

[11] C. Canuto, M. Y. Hussaini, A. Quarteroni, and T. A. Zang, *Spectral Methods in Fluid Dynamics* (Springer-Verlag, New York, 1987).

[12] H. Vandeven, "Family of spectral filters for discontinuous problems," J. Sci. Comput. **6**, 159 (1991).

[13] C.-W. Shu and S. Osher, "Efficient implementation of essentially non-oscillatory shock capturing schemes," J. Comput. Phys. **77**, 439 (1988).

[14] C.-W. Shu and S. Osher, "Efficient implementation of essentially non-oscillatory shock capturing schemes, II," J. Comput. Phys. **83**, 32 (1989).

[15] C.-W. Shu, T. A. Zang, G. Erlebacher, D. Whitaker, and S. Osher, "High order ENO schemes applied to two- and three-dimensional compressible flow," Appl. Num. Math. **9**, 45 (1992).

[16] W. E and C. W. Shu, "A numerical resolution study of high order ENO schemes applied to incompressible flows," to appear in J. Comput. Phys.

[17] G. K. Batchelor, "The stability of a large gas bubble moving through a liquid," J. Fluid Mech. **184**, 399 (1987).

[18] W. E and C. W. Shu, "Numerical study of the small scale structures in Boussinesq convection," ICASE Report No. 92-40, 1992.

[19] A. Chorin, "The evolution of a turbulent vortex," Commun. Math. Phys. **83**, 517 (1982).